Article

Microscopic Understanding of Reaction Rates Observed in Plasmon Chemistry of Nanoparticle−Ligand Systems

Robin Schürmann,* Alessandro Nagel, Sabrina Juergensen, Anisha Pathak, Stephanie Reich, Claudia Pacholski, and Ilko Bald*

Read Online

ACCESS | 📊 Metrics & More | 📖 Article Recommendations | 🆂🅸 Supporting Information

ABSTRACT: Surface-enhanced Raman scattering (SERS) is an effective and widely used technique to study chemical reactions induced or catalyzed by plasmonic substrates, since the experimental setup allows us to trigger and track the reaction simultaneously and identify the products. However, on substrates with plasmonic hotspots, the total signal mainly originates from these nanoscopic volumes with high reactivity and the information about the overall consumption remains obscure in SERS measurements. This has important implications; for example, the apparent reaction order in SERS measurements does not correlate with the real reaction order, whereas the apparent reaction rates are proportional to the real reaction rates as demonstrated by finite-difference time-domain (FDTD) simulations. We determined the electric field enhancement distribution of a gold nanoparticle (AuNP) monolayer and calculated the SERS intensities in light-driven reactions in an adsorbed self-assembled molecular monolayer on the AuNP surface. Accordingly, even if a high conversion is observed in SERS due to the high reactivity in the hotspots, most of the adsorbed molecules on the AuNP surface remain unreacted. The theoretical findings are compared with the hot-electron-induced dehalogenation of 4-bromothiophenol, indicating a time dependency of the hot-carrier concentration in plasmon-mediated reactions. To fit the kinetics of plasmon-mediated reactions in plasmonic hotspots, fractal-like kinetics are well suited to account for the inhomogeneity of reactive sites on the substrates, whereas also modified standard kinetics model allows equally well fits. The outcomes of this study are on the one hand essential to derive a mechanistic understanding of reactions on plasmonic substrates by SERS measurements and on the other hand to drive plasmonic reactions with high local precision and facilitate the engineering of chemistry on a nanoscale.
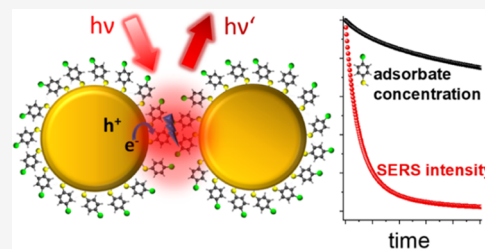
INTRODUCTION

Plasmonic nanoparticles (NPs) efficiently absorb incident light by the excitation of localized surface plasmon resonances (LSPRs), which can be exploited to drive chemical reactions in their vicinity.[1−5] The driving forces of the plasmon-mediated reactions can be either the elevated electric fields of the LSPRs or "hot" charge carriers and high temperatures at the NP surface, which are generated in the decay of the LSPRs.[6−12] Due to the action of LSPRs, the electric field in the vicinity of the NPs is significantly enhanced up to several orders of magnitude, especially when the LSPRs of NPs in close proximity are coupled and form the so-called "hotspot" in their center.[13−16] Therefore, one of the main advantages of plasmon chemistry is the ability to focus light on the nanoscale and drive chemical reactions with a local precision of a few nanometers, which allows us to engineer novel materials.[17−21] Furthermore, plasmon chemistry provides the possibility to convert solar light into chemical energy for the purpose of chemical synthesis and solar energy storage.[22−25] While strong local confinement of reactive spots is required for nanoscale engineering, it limits the overall conversion of reactions and can act as a bottleneck for the efficient use of plasmonic materials in catalytical applications. In consequence, an understanding of the processes, kinetics, and local reactivity in plasmonic chemistry is of utmost importance.

The high local field enhancement of plasmonic NPs is also used in analytical techniques like surface-enhanced Raman scattering (SERS), as the signal intensity depends significantly on the local electric field enhancement.[26−29] In this way, the generally poor cross section of Raman scattering is overcome and the vibrational fingerprint allows us to unambiguously identify molecular species up to a single-molecule level.[30] It has been demonstrated previously that chemical hotspots, areas with high reactivity, correlate with optical hotspots, namely, areas with high electric field enhancement.[17] Therefore, SERS is a widely used technique to study light-induced reactions on plasmonic substrates, since the reactions can be triggered and tracked simultaneously and the reaction products can be identified.[31−38] However, the inhomogeneous distribution of
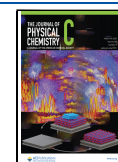
hotspots on the nanoscale typically hampers the quantitative analysis of the reaction by SERS, as a large proportion of the signal originates from the hotspots with high reactivity and hardly any signal from areas with low reactivity is observed.[39−41] Moreover, it raises the question of whether reaction parameters like reaction constant and order can be still extracted from the SERS measurements and how the overall chemical conversion of reactants on the NP surface is disguised by the plasmonic enhancement.[42] To date, several studies have been published that deal with different approaches that consider the inhomogeneity of the plasmonic substrate to deal with the kinetics in plasmon-driven reactions monitored by SERS.[33−38] One approach is fractal-like kinetics, which is typically applicable to systems with limited mobility of the reactants, leading to a time dependency of the reaction rates.[33,36−38,43] On the other hand, including an offset into the reactant signal intensities, which reflects a residual intensity after long reaction times, allows us to fit the SERS data with standard reaction kinetics equally well, even though the origin of this residual intensity still remains speculative.[34,35]

To systematically elucidate the role of the inhomogeneous plasmonic properties in the observed reaction kinetics in SERS measurements, the SERS intensities of reactants in plasmon-driven reactions adsorbed on AuNP substrates are simulated within this work. For reactions driven by the local fields or by the transfer of hot carriers, the intensity and concentration of the reactants are determined and compared with experimental SERS measurements on AuNP monolayers under illumination for different reaction orders, reaction constants, and excitation wavelengths.

METHODS

FDTD Simulation and Data Processing. Finite-difference time-domain (FDTD) simulations of the AuNP monolayer on a Si substrate are carried out using the software Lumerical FDTD Solutions 8.6.3 with a mesh size of 0.5 nm. The Si substrate was covered with a 2 nm SiO_2 layer and decorated with a single layer of AuNPs with a gap distance of 1.8 nm. Periodic boundary conditions in the x–z- and y–z-plane and PML boundary conditions in the x–y-plane are applied on a unit cell containing two AuNPs to simulate a homogeneous monolayer. A linear polarized plane-wave source of a single wavelength (488, 532, 633, and 785 nm) is used to irradiate the sample from the top. The calculated electric fields are normalized to the electric field of the light source E_0; hence, the incident energy for different wavelengths is the same.[17] E-field monitors are placed at equal distances along the z-axis of the AuNPs. The simulated E-field images are exported to Matlab (R2019a), where all pixels in a radius of around 1 nm are extracted and exported to Origin 9.1 software, where histograms of E/E_0 are plotted. Based on the histograms, the intensities I_{sim} are calculated according to the procedures described in the results part. Reflectance R and transmission T of the AuNP monolayer are determined by evaluating the power below the AuNP and above a plane-wave light source (400−900 nm) with power monitors. The absorption is given by $A = 1 − R − T$.

AuNP Substrate Synthesis. NP monolayers were synthesized by a modified method known from the literature:[44] Silicon substrates (2 cm × 2 cm, 1−5 Ω·cm, p-type, single-side polished) were purified for 24 h in piranha solution (3:1 mixture of H_2SO_4 (96%) and H_2O_2 (30%)) and then rinsed with deionized water and dried in a stream of N_2. Twelve

milliliters of a gold NP dispersion (NP diameter: 40 nm) with an absorbance of 1.0 was concentrated to 1 mL by centrifugation. A silicon substrate was placed in a 25 mL beaker and 4.5 mL of a solution containing oleylamine in hexane (10.4 μM) was added to the substrate. Then, 1 mL of the concentrated NP solution was placed onto the polished side of the Si substrate to form a convex droplet. Afterward, 0.5 mL of ethanol was added to the solution at a rate of 0.1 mL/min using a syringe pump. While ethanol was dropped into the solution, the formation of small NP monolayer islands above the Si substrate at the water/hexane interface was observed. With time, the transfer of the islands occurred from the water/oil interface to the water/air interface. After the completion of ethanol addition, the solution was allowed to rest for 10 min. Then, the entire solution was removed at a rate of 0.1 mL/min using a syringe pump so that the NP monolayer was transferred onto the Si substrate surface. The AuNP monolayer substrate was incubated in 200 μM BrTP solution overnight and subsequently placed in a bath with EtOH to remove unbound BrTP (Table 1).

Table 1. Overview of Substances Used in the Present Study along with the Supplier and Purity

chemicals	supplier	purity [%]
AuNP (40 nm) dispersion	BBI	
4-bromothiophenol	Alfa Aesar	98
ethanol	Carl Roth	≥99.8
hexane	Sigma-Aldrich	>97
oleylamine	Acros Organics	80−90

Chemicals. Raman Measurements. Raman measurements were performed with a Witec alpha 300 confocal Raman microscope using excitation lasers of 532, 633, and 785 nm wavelengths, which are focused on the sample by a Nikon E-Plan objective (50×, 0.75). All SERS spectra were further processed using WITec Project 5.1 and Origin 9.1 software.

Microabsorbance Measurements. The microabsorbance spectra were recorded with a microabsorbance spectrometer, which is described elsewhere in detail.[45,46] Thereby, light from a supercontinuum laser (Fianium, SC-400-4) was guided through a beamsplitter to a modified microscope and focused on the sample with an Olympus SLMPlan FLN 20× objective with an NA of 0.25. With the same objective, the reflected light was collected and guided by an optical fiber (Oceans Optics QP600-2-UV-BX) to a spectrometer (Avantes, Avaspec 3648). The microabsorbance spectra were measured at several places of the sample. The reflectance of the Si substrate[47] close to the measurement position was used as a reference $I_{reference}$ for reflection. With $R = \frac{I_{sample} - I_{dark}}{I_{reference} - I_{dark}}$, the reflectance was calculated. Since no light was transmitted through the Si wafer, the transmittance T could be neglected and the absorbance A was given by $A = 1 − R$.

RESULTS AND DISCUSSION

Electric Field Enhancement Factor Distribution on the AuNP Surface. To simulate SERS intensities I_{SERS}, the electric field enhancement (E/E_0) on the surface of the AuNPs is determined in the first step, since I_{SERS} depends on the power of four on (E/E_0)

$$I_{SERS} \propto (E/E_0)^4 \cdot I_0 \qquad (1)$$

Scheme 1. Schematic Representation of the Data Processing of the FDTD-Simulated Enhancement Factors E/E_0[a]
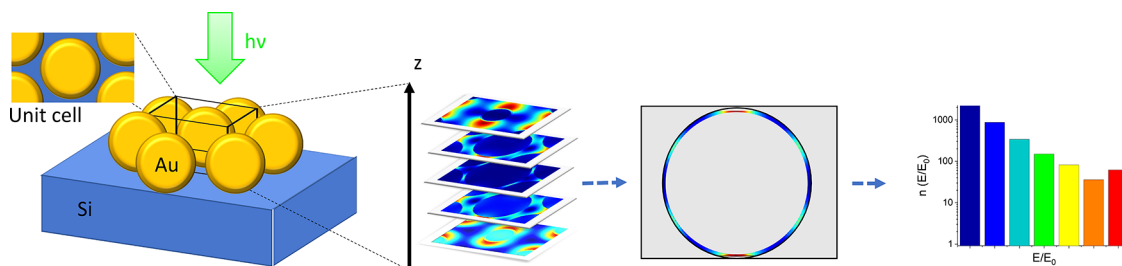
[a]In the first step, the illuminated AuNP monolayer is simulated with periodic boundary conditions and E/E_0 is determined for $x-y$-slides along the z-axis. Pixels in a 1 nm radius around the AuNP are extracted and plotted as a histogram of E/E_0, revealing the distribution of enhancement factors on the AuNP surface.
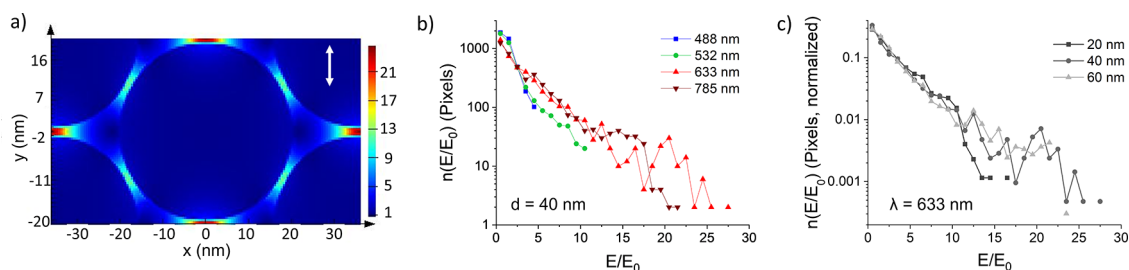

Figure 1. (a) E/E_0 in the $x-y$-plane through the center of a 40 nm AuNP monolayer on a Si substrate under 633 nm illumination simulated by FDTD. White arrow shows the polarization of the light. (b) Histogram of $n(E/E_0)$, which is the number of pixels with a certain enhancement E/E_0, as a function of E/E_0 in a 1 nm wide area around the AuNP surface under illumination with 488, 532, 633, and 785 nm light. (c) $n(E/E_0)$ vs E/E_0 for the AuNP monolayer for different AuNP sizes (20, 40, and 60 nm) under illumination with 633 nm light.

where I_0 is the intensity of the incident light.[27] In Scheme 1, the general procedure to determine the distribution of (E/E_0) using the finite-difference time-domain (FDTD) simulations is presented. As a model substrate, a densely packed monolayer of 40 nm AuNPs separated by 1.8 nm located on a Si substrate with a 2 nm SiO_2 layer is chosen and E/E_0 is simulated in a unit cell containing two AuNPs with periodic boundary conditions under illumination with a plane-wave light source. E/E_0 is determined in 17 $x-y$-planes along the z-axis of the AuNPs, and the E/E_0 values in a distance up to 1 nm around the AuNP surface are extracted, which represents the localization of small adsorbed molecules on the AuNP surface. In this way, the distribution of the electric field enhancement $n(E/E_0)$ in the molecular layer at the AuNP surface is determined, which is the number of pixels with a certain enhancement (E/E_0).

Figure 1a shows the E/E_0 in the $x-y$-plane through the center of a 40 nm AuNP monolayer under illumination with 633 nm light. In the interspace of the neighboring AuNPs along the polarization axis of the incident light, hotspots are formed, where E/E_0 can reach above 20, which corresponds to a SERS enhancement of more than 10^5. However, on most of the AuNP surface, the electric field enhancement is relatively moderate. For typical laser wavelengths used in Raman microscopes (488, 532, 633, and 785 nm), the distribution $n(E/E_0)$ is determined, showing a high enhancement at 633 and 785 nm, low enhancement at 532 nm, and even lower enhancement at 488 nm (see Figure 1b). Moreover, substrates composed of NPs with 20, 40, and 60 nm diameters are simulated, showing the highest enhancement for AuNPs with diameters of 40 and 60 nm (see Figure 1c).

In the following, the SERS intensity I_{sim} of 40 nm AuNP monolayers is calculated by summation over all molecules in the laser spot. Hence, I_{sim} can be written as

$$I_{sim} = \sum_{(E/E_0)} n(E/E_0) \cdot (E/E_0)^4 \cdot I_{Raman} \quad (2)$$

where I_{Raman} is the normal Raman signal of the adsorbed molecules in the absence of AuNPs.

Reactions on the AuNP Surface. To simulate the SERS intensity in the course of an ongoing reaction in an immobile molecular monolayer on the AuNP surface, it is assumed that the local reaction constant k^* is a function of the local light intensity and consequently depends on $(E/E_0)^2$

$$k^* = k \cdot (E/E_0)^2 \quad (3)$$

This reflects the situation in photon-induced reactions, such as photobleaching, and reactions triggered by a direct electron transfer in chemically induced damping, where a single photon triggers a reaction by electronic excitation or electron transfer. Nevertheless, it needs to be mentioned that this model does not reflect well the situation of thermally driven and indirect hot-carrier-transfer reactions, where the electrons or holes migrate a certain distance after generation before being transferred to the adsorbed molecules. It is assumed that the initial concentration of molecules c_0 is homogeneous on the surface, as in the case of self-assembled molecular monolayers, like thiophenol derivatives. Consequently, for a first-order reaction, e.g., the hot-electron-induced dehalogenation of molecules,[33,35,36] the local concentration of molecules $c(t)$ is given by

$$c(t) = c_0 \cdot e^{-k^* \cdot t} \quad (4)$$

The intensity of the Raman signal is proportional to the number of molecules in the observed volume and in consequence also to their local concentration: $I_{Raman} \propto c(t)$. As the simulated intensity I_{sim} is given in an arbitrary unit, the
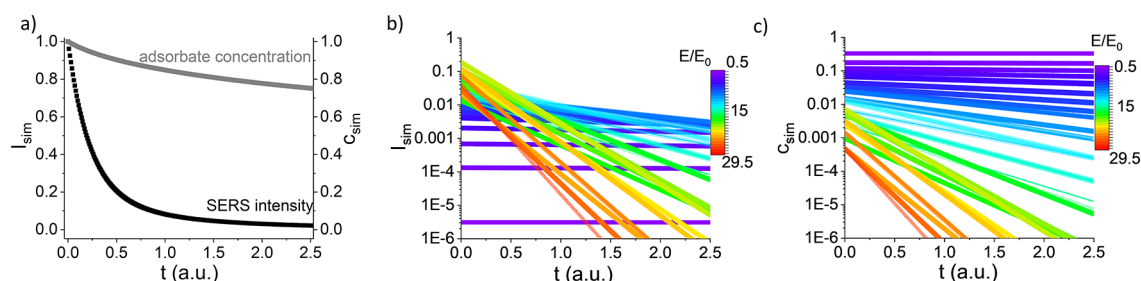
Figure 2. (a) $I_{sim}(t)$ (black) and $c_{sim}(t)$ (gray) plotted as a function of time, which is calculated for a first-order reaction on a 40 nm AuNP monolayer illuminated with 633 nm light. (b) $I_{sim}(t)$ of the same substrate as in (a) plotted individually for each enhancement factor E/E_0 (given by color code). (c) $c_{sim}(t)$ of the same substrate as in (a) plotted individually for each enhancement factor E/E_0.

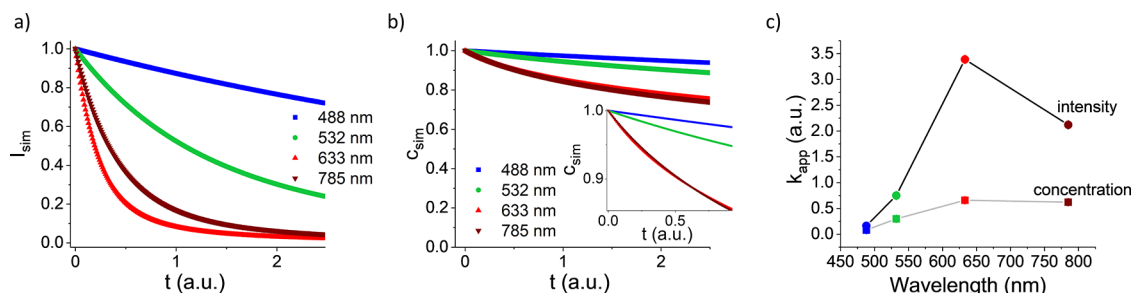**Figure 3.** (a) $I_{sim}(t)$ of a first-order reaction of molecules on a 40 nm AuNP monolayer illuminated with 488, 532, 633, and 785 nm light. (b) $c_{sim}(t)$ of the same system as in (a). Inset shows short illumination times. (c) Observed reaction rates k_{app} plotted as a function of the wavelength of the incident light, determined by fitting the data in (a) and (b) with an exponential decay function $I = I_0 \cdot e^{-kt}$.

proportionality factor between I_{Raman} and $c(t)$ can be neglected. In this way, the SERS intensity can be calculated by combining eqs 2−4

$$I_{sim}(t) = \sum_{(E/E_0)} n_{(E/E_0)}(E/E_0)^4 \cdot e^{-k \cdot (E/E_0)^2 \cdot t} \tag{5}$$

However, I_{sim} does not reflect the concentration of reactants in the system, as the molecules on the surface experience nonuniform enhancement; thus, the concentration in the course of the reaction is given by

$$c_{sim}(t) = \sum_{(E/E_0)} n_{(E/E_0)} \cdot e^{-k \cdot (E/E_0)^2 \cdot t} \tag{6}$$

In Figure 2a, $I_{sim}(t)$ and $c_{sim}(t)$ are plotted for a first-order reaction on a 40 nm AuNP monolayer under illumination with 633 nm light, showing a rapid decrease in $I_{sim}(t)$. On the contrary, $c_{sim}(t)$ decreases only slightly, even when the SERS signal almost vanishes. To elucidate the discrepancy between the overall values of $I_{sim}(t)$ and $c_{sim}(t)$, $I_{sim}(t)$ and $c_{sim}(t)$ from areas experiencing a certain enhancement factor (E/E_0) on the AuNP surface are shown in Figure 2b,c individually. In Figure 2b, it is obvious that most of the signal $I_{sim}(t)$ originates from areas with a high E/E_0, where the signal rapidly decays, whereas areas with no or poor E-field enhancement hardly contribute to the overall signal. However, the concentration of molecules $c_{sim}(t)$ plotted in Figure 2c for the individual E/E_0 values reveals that the majority of molecules are located in mainly unreactive areas with poor enhancement and only a few are located in the regions with high enhancement. This leads to the conclusion that the observed reaction is mainly limited to a very small volume, whereas the majority of the molecules on the AuNP surface are hardly affected. Thus, in the studied system, the reactants, hot carriers, or photons on the one side and adsorbed molecules on the other side, unmix due to their

limited mobility. With progress in reaction time, the molecules in the reactive hotspots are mostly converted, whereas the majority of molecules remain unreacted on the poorly reactive sides of AuNPs. This effect can be exploited to drive reactions on defined locations on the AuNP surface with high precision; moreover, the position of the hotspots can be changed by changing the polarization angle of the incident light and certain spots on the surface can be addressed independently (see Figure S1).

Wavelength Dependency. Kinetic studies of plasmon-mediated reactions were performed previously by several groups as a function of the excitation wavelength to elucidate the reaction mechanism.[10,35,36]

In Figure 3a $I_{sim}(t)$ is shown for the illumination with different laser wavelengths, revealing a significant impact of wavelength on the signal decrease, even though all other parameters of the simulation are equal. The rate of the signal decrease obviously follows the order 488 < 532 < 785 < 633 nm, which correlates with the highest observed enhancement factors in Figure 1b. The concentrations c_{sim} are plotted in Figure 3b as a function of time and show a less pronounced decrease compared to I_{sim} following the order 488 < 532 < 633 < 785 nm. Most remarkable is that for 633 nm, the intensity drop (giving rise to an "apparent rate") is faster than that for 785 nm, while the actual drop in molecular concentration (corresponding to a "real reaction rate") on the surface is slightly faster for 785 nm at longer illumination times. The reaction constants k are determined from $I_{sim}(t)$ and $c_{sim}(t)$ by exponential fits ($I = I_0 \cdot e^{-kt}$ and $c = c_0 \cdot e^{-kt}$) and are presented in Figure 3c, revealing a lack of correlation between values determined from $I_{sim}(t)$ and $c_{sim}(t)$, respectively, for different wavelengths. The discrepancy of the k values at 633 and 785 nm is mainly caused by the differences in the distribution of high values of E/E_0 for individual wavelengths (see Figure 1b), since irradiation at 633 nm results in strong but locally
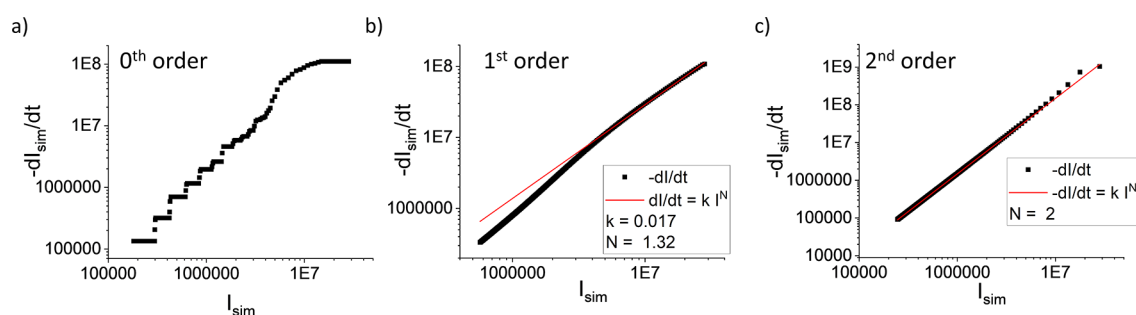
Figure 4. $-dI_{sim}/dt$ plotted as a function of I_{sim} of a 40 nm AuNP monolayer illuminated with 633 nm light for a zeroth-order (a), first-order (b), and second-order (c) reactions fitted with $dI_{sim}/dt = -k \cdot I_{sim}^N$ to determine the apparent reaction order N.
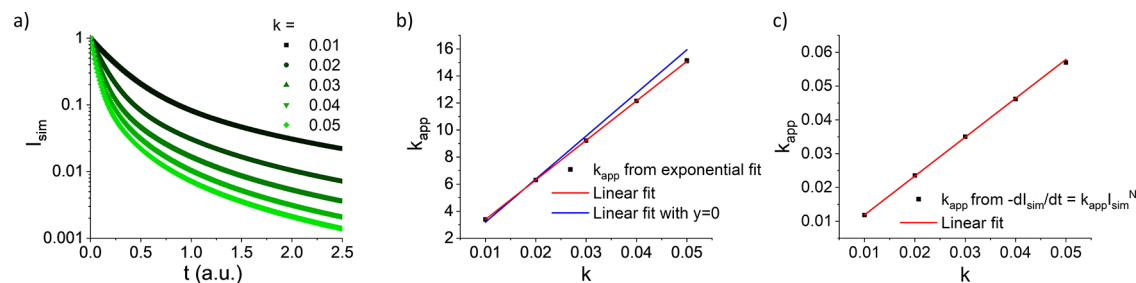

Figure 5. (a) I_{sim} of molecules decaying in a first-order reaction with different reaction constants k on a 40 nm AuNP monolayer under illumination with 633 nm photons plotted in log scale as a function of time. (b) Reaction constants k_{app} determined from I_{sim} presented in (a) plotted vs k. (c) k of data shown in (a) obtained by fitting $-dI_{sim}/dt$ vs I_{sim} plot with N fixed to 4/3 plotted vs k.

confined hotspots, whereas the enhancement of the majority of the pixels is higher for a 785 nm illumination. Hence, the rate constants determined on the same substrate under equal conditions are not fully comparable for different excitation wavelengths, since the spatial extension of the hotspots needs to be considered. In principle, the extension of the reactive sites could be slightly controlled by the selection of the excitation wavelength (see Figure S2 for FDTD data); however, since the excitation wavelength influences the plasmon-mediated reactions in a manifold manner, which will be discussed later on, the applicability of this effect remains unclear.

Here, for all wavelengths, the same reaction constant k is used; however, under experimental conditions, k significantly depends on the incident wavelength. In hot-electron-transfer reactions, the electronic states together with the photon energy determine the electron-transfer probability; moreover, the absorption of the AuNPs determines the formation of hot charge carriers. For the present AuNP monolayer, the absorption is determined by FDTD simulations and shows high absorption at 488 and 532 nm and low absorption at 633 and 785 nm (see Supporting Information 2e), which affect k in the hot carrier and thermally influenced reactions. Furthermore, in photobleaching reactions also, the reaction rates are highly dependent on the electronic structure of the molecules and the wavelength of the incident light.

Reaction Order. In reaction kinetics, the reaction order is of utmost importance to understand the temporal behavior of the overall consumption and the underlying reaction mechanism. Therefore, in addition to the first-order reactions discussed above, zeroth- and second-order reactions are simulated as well with the local $c_{sim}(t)$ given by

$$\text{0th order} \quad c(t) = c_0 - k^* \cdot t \tag{7}$$

$$\text{2nd order} \quad c(t) = \frac{c_0}{1 + c_0 \cdot k^* \cdot t} \tag{8}$$

In general, the reaction order N is given by the rate equation[48]

$$dc/dt = -k \cdot c^N \tag{9}$$

In Figure 4, $-dI_{sim}/dt$ is plotted as a function of I_{sim} to determine the apparent reaction order of zeroth-, first-, and second-order reactions on the 40 nm AuNP monolayer in the case of 633 nm illumination. Usually, dI_{sim}/dt is constant for a zeroth-order reaction; nevertheless, in the case of the zeroth-order reaction on the plasmonic substrate, the derivative of the intensity is clearly time-dependent (see Figure 4a). The reason is that after a certain time, the reaction is already completed in regions with high enhancement, while it is still ongoing in other areas with a lower local reaction rate k^*. The steps in the plots are artifacts of the calculation, as the enhancement factors of the individual spots are grouped according to the histogram plot in Figure 1b. For the first-order plot in Figure 4b, the apparent reaction order deviates from the first order and is around 4/3 with some further deviations for long irradiation times. The order of 4/3 matches well the expected value for a first-order reaction on a substrate with an exponential distribution of $n(E/E_0)^2$, which is described in more detail in the SI. Interestingly, the reaction order determined from dc/dt of the overall reaction deviates from both the local first order of the reaction and the apparent reaction order determined from dI_{sim}/dt (see Figure S4). Nevertheless, for a second-order reaction, the apparent reaction order agrees well with the underlying local reaction order, as shown in Figure 4c and explained in SI. Hence, caution is particularly required when drawing conclusions about the reaction order from SERS measurements of plasmon-mediated reactions, since especially for zeroth- and first-order reactions, there is a mismatch between the apparent reaction order, the reaction order of the
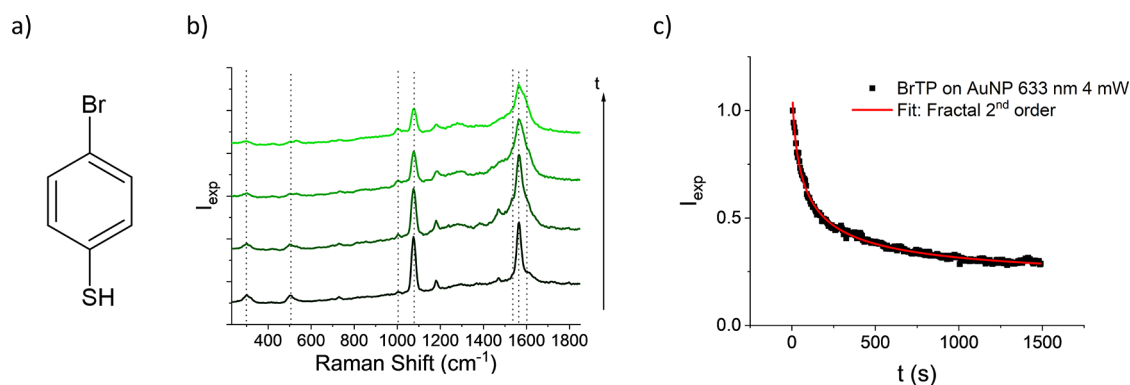
Figure 6. (a) Molecular structure of BrTP. (b) Raman spectra of BrTP on AuNP monolayer after different illumination times (633 nm, 4 mW, 50×). (c) Intensity of a 1076 cm^{-1} peak is plotted as a function of the illumination time and fitted with a second-order fractal reaction.
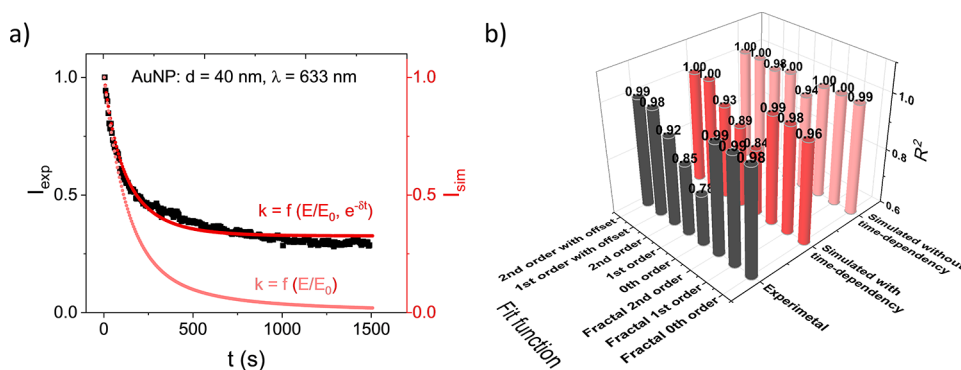

Figure 7. (a) Calculation of the first-order reaction with (red) and without (light red) an exponential time dependency of hot carriers and experimental intensity of 1076 cm^{-1} BrTP peak as a function of time (black, data shown in Figure 6c). (b) R^2 values for different fitting functions for first-order reactions on a 40 nm AuNP substrate illuminated with 633 nm light determined by simulations with and without taking an exponential dependency of the hot-carrier concentration into account and by experimental SERS measurements.

underlying reaction mechanism, and the order of the real reaction on the surface.

Rate Constant. In addition to the reaction order, the rate constant is the quantity defining the reaction rate. In Figure 5a, I_{sim} for different first-order rate constants k is plotted, clearly showing that the apparent reaction does not follow the expected exponential trend for first-order reactions. By fitting the I_{sim} with an exponential function $I_{sim} = I_{sim}(t = 0) \cdot e^{-k \cdot t} + I_{sim}(t = \infty)$, the apparent rate constants k_{app} are determined. These are presented in Figure 5b as a function of the rate constants k. There is a linear correlation between k and k_{app} constants; hence, the apparent rate constants k_{app} determined from SERS measurements are comparable, e.g., in laser power series or for different molecular reactions on the same substrate. Furthermore, k_{app} is determined as well from the $-dI_{sim}/dt$ versus I_{sim} plots with $N = 4/3$ (shown in Figure 4b) and plotted as a function of k (see Figure 5c). In this way, the k values of a first-order reaction can be extracted from SERS measurements, which allows us to conclude about the reaction rates on the poorly enhanced areas of the AuNP surface if the electric field enhancement and the reaction mechanism are known, which remain typically obscure in SERS.

Dehalogenation Kinetics in Experimental SERS Measurements. To compare the findings for the simulated intensity I_{sim} with the experimental value I_{exp}, the decomposition of 4-bromothiophenol (BrTP) (see Figure 6a) on a 40 nm AuNP monolayer is monitored with SERS as a model reaction. Scanning electron microscopy (SEM) images of the AuNP monolayer substrates shown in Figure S5 show a

densely packed single layer of NPs on a Si substrate. BrTP is chosen as a model compound, as on the one hand it forms a self-assembled monolayer on the metal surface and on the other hand cleaves efficiently the carbon−bromide bond upon attachment of electrons with an energy close to 0 eV[49−52]

$$BrTP + e^- \rightarrow Br^- + TP\cdot$$
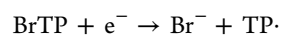
In addition to the electron-induced dehalogenation, subsequent intermolecular coupling reactions of thiophenol derivatives have been observed previously on plasmonic substrates.[53,54]

In Figure 6b, Raman spectra of BrTP on the AuNP monolayers under illumination with a 633 nm laser (4 mW, 50×) of a confocal Raman microscope are shown. The first recorded spectrum (black) after 5 s illumination shows mainly the vibrational fingerprint of BrTP,[55] with its characteristic peaks at 302 cm^{-1} (C−Br stretch and ring deformation), 507 cm^{-1} (ring deformation), 1076 cm^{-1} (ring stretch), 1181 cm^{-1} (C−H deformation), and 1565 cm^{-1} (C−C stretch).[56] As illumination time increases, new peaks emerge, e.g., the 1005 cm^{-1} peak, which can be assigned to the formation of thiophenol (TP).[57,58] Furthermore, a strong broadening of and a relative increase in the 1565 cm^{-1} peak are observed, which are assigned to the C−C ring vibration[54] and are most likely caused by the reaction of the TP derivatives with neighboring molecules, forming biphenol species[54] and amorphous networks.[53,59] To determine the decomposition of BrTP, the intensity of the ring stretching vibration at 1076 cm^{-1} is plotted as a function of time (see Figure 6c) and exemplary
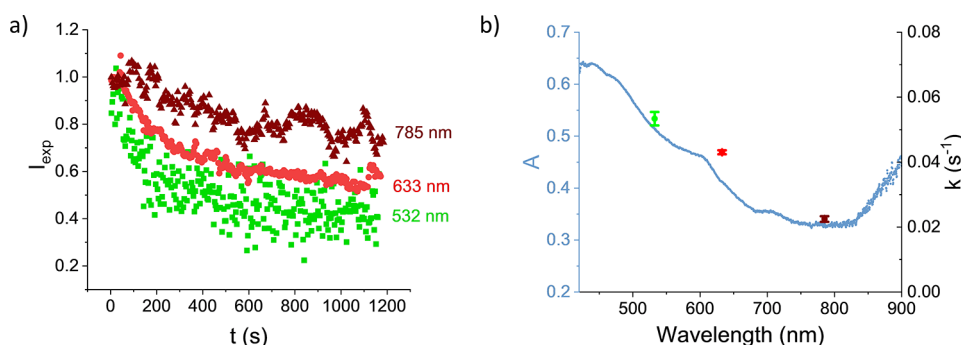
Figure 8. (a) Intensities of 1076 cm^{-1} peak under illumination with 1 mW light of 532 nm (green), 633 nm (red), and 785 nm (dark red) wavelengths. The scattering at different wavelengths is related to the different absolute signal intensities of the Raman measurements due to the wavelength dependency of the plasmonic enhancement. (b) Absorbance (A) (blue line) determined by microabsorbance measurements of the 40 nm AuNP monolayer. The absorbance is plotted together with k values (colored dots) determined from the SERS data presented in (a).

fitted with second-order fractal kinetics.[37,43] To exclude the effects of spectral overlaps of the 1076 cm^{-1} peak with the signals from possible reactions products, the intensities of the less intense peaks at 302 and 507 cm^{-1} are plotted as well, which show the same decomposition kinetics (see Figure S6). As illumination time increases, the SERS signal of BrTP seems to converge to a residual intensity, which is already observed previously for reactions on plasmonic substrates[33−35] but not in the simulations described above.

Time Dependency of Hot Carriers. In the simulations, it is assumed so far that the generation and transport of hot carriers are time-independent. Under a constant concentration of hot carriers, the I_{sim} of the reactants approaches zero with the increase in illumination time (see Figure 7a), which is observed in the experimental data (see Figure 6c) and might be explained by the time dependency of the electron transfer in the experiment. With the increase in illumination time, an accumulation of charges in the molecular layer is likely and further electron transfer from the AuNPs to the molecules is consequently hampered. Therefore, the concentration of hot carriers decreases with the increase in illumination time. In the following, the expected time dependency of the local hot-carrier concentration is implemented by an exponential decrease in the hot-carrier concentration, leading to $k = f(E/E_0, e^{-\delta t})$. The exponential time dependency is assumed for a simple donor−acceptor model of the electron transfer,[60] whereas other time-dependency models also lead to comparable results (see Table S1).

In Figure 7a, the intensity I_{exp} of the 1076 cm^{-1} peak of BrTP under illumination with 633 nm light (50× objective, 4 mW) is plotted together with simulated intensity curves with and without a time-dependent decrease in hot electrons. The curves with a time-dependent decrease in hot electrons match the experimental data quite well at all times, whereas those without a time dependency I_{sim} only match the experimental data for short illumination times and approach zero for long times.

Furthermore, I_{sim} is simulated for a first-order reaction with time-independent and time-dependent rate coefficients and is fitted with different functions. The R^2 values of the fits of the simulated intensities are presented in Figure 7b together with the fits of experimental SERS data for the dehalogenation of BrTP. The zeroth-, first- and second-order kinetics (eqs 4, 7, and 8, respectively) are applied with and without an additional intensity offset, which reflects a residual signal intensity after long reaction times. Moreover, fractal-like kinetics[43] of zeroth-,

first-, or second-order reactions, which takes the inhomogeneity of the substrate into account, are used to fit the data with $k = k_f t^{-h}$, and the intensities are given by

0th order fractal $I = I_0 - k_f \cdot t^{-h}$ (10)

1st order fractal $I = I_0 \cdot \dfrac{e^{k_f \cdot t^{(1-h)}}}{(1-h)}$ (11)

2nd order fractal $I = \dfrac{I_0 \cdot (1-h)}{(1-h) + I_0 \cdot k_f \cdot t^{(1-h)}}$ (12)

The R^2 values shown in Figure 7b indicate that fractal-like kinetics or standard kinetics equations with an additional offset fit the simulated intensities well. It is most remarkable that even though the underlying reaction is first order, in all cases, the fits give similar R^2 values independent of the reaction order of the fit. For the different reaction orders, only minor differences can be observed, whereas the type of kinetics, whether fractal-like or standard, has a greater influence on the quality of fits. In consequence, hardly any conclusion about the reaction order based on the fitting of I_{sim} can be drawn.

Fractal-like kinetics takes the inhomogeneity of the substrate by a time-dependent reaction coefficient into account and fits all studied time-dependent and time-independent systems with high accuracy. It needs to be mentioned that the physical meaning of h, which is generally connected with the fractal dimension of the system, is not fully understood. The inhomogeneity of the substrate in the present case is not caused by a fractal-shaped substrate with limited mobility of reactants but by the distribution of local reaction rates, which are already present within a single hotspot or even a single particle illuminated with polarized light. Nevertheless, the determined reaction coefficients k_f depend linearly on the reaction constant; thus, this approach is well suited to fit SERS intensities to determine reaction kinetics (see Figure S7). On a homogeneous substrate, a thermally driven reaction follows standard kinetics due to the fast heat dissipation within the AuNPs. However, inhomogeneities in the alignment of the AuNPs may lead to inhomogeneous heating of the individual particles,[61,62] which leads to an inhomogeneous distribution of local reaction rates on the substrate and favor the use of fractal kinetics.

In practically all cases, the use of an additional residual intensity fits the data much better than the standard kinetics equations and comparably well like fractal kinetics. In the

present simulations, the remaining signal intensity corresponds to a charge accumulation in the molecular layer, slowing down the electron-transfer rate. Nevertheless, in a recent work of Sarhan et al., where a thermally-driven reaction mechanism in which the role of hotspots can be neglected and standard kinetics models can be applied was assumed, the offset was rationalized by unreactive sides on the AuNP surface.[63] Also, in hot-electron-induced reactions, less-reactive sites in the optical hotspots may explain the offset, which are due to a different density of states or an insulating layer. Hence, in experimental measurements, additional information about the underlying reaction mechanism and the nanoscopic properties of the plasmonic substrate is required to interpret the observed reaction parameter.

Role of Absorption in Reaction Kinetics. In Figure 8a, the intensity of the BrTP signal at 1076 cm^{-1} is shown for illumination with 532, 633, and 785 nm laser light, revealing the highest reaction rate for 532 nm, followed by 633 and 785 nm. For 488 nm illumination, no SERS signal could be detected due to the poor signal enhancement.

This indicates that the underlying reaction rate k significantly depends on the wavelength of the incident laser light, e.g., due to the electron-transfer probability determined by the density of states.[38] However, based on the FDTD simulations shown in Figure 3a, a different wavelength dependency based on the plasmonic substrate could be expected. Microabsorbance measurements of the 40 nm AuNP monolayer reveal that the absorbance A of the substrate decreases with the wavelength of the light (see Figure 8b). Therefore, high reaction rates can be explained by the higher absorbance of the AuNP substrate, leading to an increased generation of hot carriers, which obviously has a higher impact on k than the local E-field enhancement.

CONCLUSIONS

This study shows that reactions induced by photons or hot carriers on an illuminated plasmonic substrate are mainly driven in a spatially highly confined area with a high electric field enhancement, whereas the majority of the AuNP's surface is mainly unreactive. Consequently, the conversion of molecules like thiophenol derivatives, which are tightly bound to the AuNP surface, is highly limited. In SERS measurements, mainly the signal of these reactive hotspots is monitored, whereas the information about the molecules on the residual surface is disguised. The extension and position of the hotspots can be adjusted by the wavelength and polarization of the exciting laser, whereby for the reactivity in the hotspots, the absorbance is more crucial than the local field enhancement, as shown by microabsorbance measurements. This gives the opportunity to tailor locally defined reactions on the NP surface with a nanometer precision. For analytical applications of SERS, it must be considered that the underlying reaction parameters like order and rate are concealed by the inhomogeneous signal enhancement. It is demonstrated that apparent reaction orders and rates may deviate from the underlying reaction parameters; however, the apparent rate constants are proportional to the underlying rate constants for the same substrate and laser wavelength. Using fractal-like kinetics, the SERS intensity of plasmon-mediated reactions can be fitted with high accuracy, as the inhomogeneity of the reactivity of the substrate is considered to be a time-dependent rate coefficient. The observed asymptotic intensity at long irradiation times of the reactants

SERS signal in plasmon-driven reactions could be explained by a time dependency of the hot-carrier transfer caused by the accumulation of charges in the molecular layer. These findings are crucial for a correct interpretation of the reaction kinetics in plasmon-mediated reactions monitored by SERS and moreover pave the way for nanoscale chemistry on plasmonic substrates.

◼ ASSOCIATED CONTENT

ⓈI Supporting Information

The Supporting Information is available free of charge at https://pubs.acs.org/doi/10.1021/acs.jpcc.2c00278.

FDTD simulations of the AuNP monolayer at different wavelengths and polarizations; detailed derivation of the reaction kinetics; scanning electron microscopy images of the AuNP monolayer; Raman intensities of individual peaks as a function of time; reaction rates determined by fractal kinetics; and R^2 values of kinetics fit functions (PDF)

◼ AUTHOR INFORMATION

Corresponding Authors

Robin Schürmann − *Institute of Chemistry, University of Potsdam, D-14476 Potsdam, Germany*; Email: rschuerm@uni-potsdam.de

Ilko Bald − *Institute of Chemistry, University of Potsdam, D-14476 Potsdam, Germany*; ◉ orcid.org/0000-0002-6683-5065; Email: bald@uni-potsdam.de

Authors

Alessandro Nagel − *Institute of Chemistry, University of Potsdam, D-14476 Potsdam, Germany*

Sabrina Juergensen − *Department of Physics, Freie Universität Berlin, D-14195 Berlin, Germany*

Anisha Pathak − *Institute of Chemistry, University of Potsdam, D-14476 Potsdam, Germany*

Stephanie Reich − *Department of Physics, Freie Universität Berlin, D-14195 Berlin, Germany*

Claudia Pacholski − *Institute of Chemistry, University of Potsdam, D-14476 Potsdam, Germany*; ◉ orcid.org/0000-0003-1620-5783

Complete contact information is available at:
https://pubs.acs.org/10.1021/acs.jpcc.2c00278

Notes

The authors declare no competing financial interest.

◼ ABBREVIATIONS

AuNP, gold nanoparticle; BrTP, 4-bromothiophenol; FDTD, finite-difference time domain; LSPRs, localized surface

plasmon resonances; SERS, surface-enhanced Raman scattering; TP, thiophenol

■ REFERENCES

(1) Zhang, Y.; He, S.; Guo, W.; Hu, Y.; Huang, J.; Mulcahy, J. R.; Wei, W. D. Surface-Plasmon-Driven Hot Electron Photochemistry. *Chem. Rev.* **2018**, *118*, 2927–2954.

(2) Zhan, C.; Chen, X.-J.; Yi, J.; Li, J.-F.; Wu, D.-Y.; Tian, Z.-Q. From Plasmon-Enhanced Molecular Spectroscopy to Plasmon-Mediated Chemical Reactions. *Nat. Rev. Chem.* **2018**, *2*, 216–230.

(3) Gellé, A.; Jin, T.; de la Garza, L.; Price, G. D.; Besteiro, L. V.; Moores, A. Applications of Plasmon-Enhanced Nanocatalysis to Organic Transformations. *Chem. Rev.* **2020**, *120*, 986–1041.

(4) Cortés, E.; Besteiro, L. V.; Alabastri, A.; Baldi, A.; Tagliabue, G.; Demetriadou, A.; Narang, P. Challenges in Plasmonic Catalysis. *ACS Nano* **2020**, *14*, 16202–16219.

(5) Zhang, Z.; Zhang, C.; Zheng, H.; Xu, H. Plasmon-Driven Catalysis on Molecules and Nanomaterials. *Acc. Chem. Res.* **2019**, *52*, 2506–2515.

(6) Chavez, S.; Aslam, U.; Linic, S. Design Principles for Directing Energy and Energetic Charge Flow in Multicomponent Plasmonic Nanostructures. *ACS Energy Lett.* **2018**, *3*, 1590–1596.

(7) Hartland, G. V.; Besteiro, L. V.; Johns, P.; Govorov, A. O. What's so Hot about Electrons in Metal Nanoparticles? *ACS Energy Lett.* **2017**, *2*, 1641–1653.

(8) Chang, L.; Besteiro, L. V.; Sun, J.; Santiago, E. Y.; Gray, S. K.; Wang, Z.; Govorov, A. O. Electronic Structure of the Plasmons in Metal Nanocrystals: Fundamental Limitations for the Energy Efficiency of Hot Electron Generation. *ACS Energy Lett.* **2019**, *4*, 2552–2568.

(9) Manjavacas, A.; Liu, J. G.; Kulkarni, V.; Nordlander, P. Plasmon-induced hot carriers in metallic nanoparticles. *ACS Nano* **2014**, *8*, 7630–7638.

(10) Rodio, M.; Graf, M.; Schulz, F.; Mueller, N. S.; Eich, M.; Lange, H. Experimental Evidence for Nonthermal Contributions to Plasmon-Enhanced Electrochemical Oxidation Reactions. *ACS Catal.* **2020**, *10*, 2345–2353.

(11) Boerigter, C.; Campana, R.; Morabito, M.; Linic, S. Evidence and Implications of Direct Charge Excitation as the Dominant Mechanism in Plasmon-Mediated Photocatalysis. *Nat. Commun.* **2016**, *7*, No. 10545.

(12) Kale, M. J.; Avanesian, T.; Christopher, P. Direct Photocatalysis by Plasmonic Nanostructures. *ACS Catal.* **2014**, *4*, 116–128.

(13) Yu, H.; Peng, Y.; Yang, Y.; Li, Z.-Y. Plasmon-Enhanced Light–Matter Interactions and Applications. *npj Comput. Mater.* **2019**, *5*, No. 45.

(14) Hooshmand, N.; El-Sayed, M. A. Collective Multipole Oscillations Direct the Plasmonic Coupling at the Nanojunction Interfaces. *Proc. Natl. Acad. Sci. U.S.A.* **2019**, *116*, 19299–19304.

(15) Yang, Z.-W.; Meng, L.-Y.; Lin, J.-S.; Yang, W.-M.; Radjenovic, P.; Shen, S.-X.; Xu, Q.-C.; Yang, Z.-L.; Tian, Z.-Q.; Li, J.-F. 3D Hotspots Platform for Plasmon Enhanced Raman and Second Harmonic Generation Spectroscopies and Quantitative Analysis. *Adv. Opt. Mater.* **2019**, *7*, No. 1901010.

(16) Chen, G.; Wang, Y.; Yang, M.; Xu, J.; Goh, S. J.; Pan, M.; Chen, H. Measuring Ensemble-Averaged Surface-Enhanced Raman Scattering in the Hotspots of Colloidal Nanoparticle Dimers and Trimers. *J. Am. Chem. Soc.* **2010**, *132*, 3644–3645.

(17) Cortés, E.; Xie, W.; Cambiasso, J.; Jermyn, A. S.; Sundararaman, R.; Narang, P.; Schlücker, S.; Maier, S. A. Plasmonic Hot Electron Transport Drives Nano-Localized Chemistry. *Nat. Commun.* **2017**, *8*, No. 14880.

(18) Ding, T.; Mertens, J.; Lombardi, A.; Scherman, O. A.; Baumberg, J. J. Light-Directed Tuning of Plasmon Resonances via Plasmon-Induced Polymerization Using Hot Electrons. *ACS Photonics* **2017**, *4*, 1453–1458.

(19) Pal, S.; Dutta, A.; Paul, M.; Chattopadhyay, A. Plasmon-Enhanced Chemical Reaction at the Hot Spots of End-to-End

Assembled Gold Nanorods. *J. Phys. Chem. C* **2020**, *124* (5), 3204–3210.

(20) Zhan, C.; Moskovits, M.; Tian, Z.-Q. Recent Progress and Prospects in Plasmon-Mediated Chemical Reaction. *Matter* **2020**, *3*, 42–56.

(21) Linic, S.; Chavez, S.; Elias, R. Flow and Extraction of Energy and Charge Carriers in Hybrid Plasmonic Nanostructures. *Nat. Mater.* **2021**, *20*, 916–924.

(22) Aslam, U.; Rao, V. G.; Chavez, S.; Linic, S. Catalytic Conversion of Solar to Chemical Energy on Plasmonic Metal Nanostructures. *Nat. Catal.* **2018**, *1*, 656–665.

(23) Clavero, C. Plasmon-Induced Hot-Electron Generation at Nanoparticle/Metal-Oxide Interfaces for Photovoltaic and Photocatalytic Devices. *Nat. Photonics* **2014**, *8*, 95–103.

(24) Cushing, S. K.; Wu, N. Progress and Perspectives of Plasmon-Enhanced Solar Energy Conversion. *J. Phys. Chem. Lett.* **2016**, *7*, 666–675.

(25) Linic, S.; Christopher, P.; Ingram, D. B. Plasmonic-Metal Nanostructures for Efficient Conversion of Solar to Chemical Energy. *Nat. Mater.* **2011**, *10*, 911–921.

(26) Wang, X.; Huang, S.-C.; Hu, S.; Yan, S.; Ren, B. Fundamental Understanding and Applications of Plasmon-Enhanced Raman Spectroscopy. *Nat. Rev. Phys.* **2020**, *2*, 253–271.

(27) Schlücker, S. Surface-Enhanced Raman Spectroscopy: Concepts and Chemical Applications. *Angew. Chem., Int. Ed.* **2014**, *53*, 4756–4795.

(28) Langer, J.; de Aberasturi, D. J.; Aizpurua, J.; Alvarez-Puebla, R. A.; Auguié, B.; Baumberg, J. J.; Bazan, G. C.; Bell, S. E. J.; Boisen, A.; Brolo, A. G.; et al. Present and Future of Surface-Enhanced Raman Scattering. *ACS Nano* **2020**, *14*, 28–117.

(29) Ding, S.-Y.; You, E.-M.; Tian, Z.-Q.; Moskovits, M. Electromagnetic Theories of Surface-Enhanced Raman Spectroscopy. *Chem. Soc. Rev.* **2017**, *46*, 4042–4076.

(30) Tapio, K.; Mostafa, A.; Kanehira, Y.; Suma, A.; Dutta, A.; Bald, I. A Versatile DNA Origami-Based Plasmonic Nanoantenna for Label-Free Single-Molecule Surface-Enhanced Raman Spectroscopy. *ACS Nano* **2021**, *15*, 7065–7077.

(31) Zhan, C.; Chen, X.-J.; Huang, Y.-F.; Wu, D.-Y.; Tian, Z.-Q. Plasmon-Mediated Chemical Reactions on Nanostructures Unveiled by Surface-Enhanced Raman Spectroscopy. *Acc. Chem. Res.* **2019**, *52*, 2784–2792.

(32) Li, Z.; Kurouski, D. Nanoscale Structural Characterization of Plasmon-Driven Reactions. *Nanophotonics* **2021**, *10*, 1657–1673.

(33) Schürmann, R.; Bald, I. Real-Time Monitoring of Plasmon Induced Dissociative Electron Transfer to the Potential DNA Radiosensitizer 8-Bromoadenine. *Nanoscale* **2017**, *9*, 1951–1955.

(34) Sarhan, R. M.; Koopman, W.; Schuetz, R.; Schmid, T.; Liebig, F.; Koetz, J.; Bargheer, M. The Importance of Plasmonic Heating for the Plasmon-Driven Photodimerization of 4-Nitrothiophenol. *Sci. Rep.* **2019**, *9*, No. 3060.

(35) Liu, J.; Cai, Z.-Y.; Sun, W.-X.; Wang, J.-Z.; Shen, X.-R.; Zhan, C.; Devasenathipathy, R.; Zhou, J.-Z.; Wu, D.-Y.; Mao, B.-W.; Tian, Z.-Q. Plasmonic Hot Electron-Mediated Hydrodehalogenation Kinetics on Nanostructured Ag Electrodes. *J. Am. Chem. Soc.* **2020**, *142*, 17489–17498.

(36) Dutta, A.; Schürmann, R.; Kogikoski, S.; Mueller, N. S.; Reich, S.; Bald, I. Kinetics and Mechanism of Plasmon-Driven Dehalogenation Reaction of Brominated Purine Nucleobases on Ag and Au. *ACS Catal.* **2021**, *11*, 8370–8381.

(37) Kogikoski, S., Jr.; Dutta, A.; Bald, I. Spatial Separation of Plasmonic Hot Electron Generation and a Hydrodehalogenation Reaction Center Using a DNA Wire. *ACS Nano* **2021**, *15*, 20562–20573.

(38) Schürmann, R.; Ebel, K.; Nicolas, C.; Milosavljević, A. R.; Bald, I. Role of Valence Band States and Plasmonic Enhancement in Electron-Transfer-Induced Transformation of Nitrothiophenol. *J. Phys. Chem. Lett.* **2019**, *10*, 3153–3158.

(39) Kim, N. H.; Hwang, W.; Baek, K.; Rohman, M. R.; Kim, J.; Kim, H. W.; Mun, J.; Lee, S. Y.; Yun, G.; Murray, J.; et al. Smart SERS

Hot Spots: Single Molecules Can Be Positioned in a Plasmonic Nanojunction Using Host-Guest Chemistry. *J. Am. Chem. Soc.* **2018**, *140*, 4705−4711.

(40) Lee, H. K.; Lee, Y. H.; Koh, C. S. L.; Phan-Quang, G. C.; Han, X.; Lay, C. L.; Sim, H. Y. F.; Kao, Y.-C.; An, Q.; Ling, X. Y. Designing Surface-Enhanced Raman Scattering (SERS) Platforms Beyond Hotspot Engineering: Emerging Opportunities in Analyte Manipulations and Hybrid Materials. *Chem. Soc. Rev.* **2019**, *48*, 731−756.

(41) Long, J.; Yi, H.; Li, H.; Lei, Z.; Yang, T. Reproducible Ultrahigh SERS Enhancement in Single Deterministic Hotspots Using Nanosphere-Plane Antennas Under Radially Polarized Excitation. *Sci. Rep.* **2016**, *6*, No. 33218.

(42) Bell, S. E. J.; Charron, G.; Cortés, E.; Kneipp, J.; de la Chapelle, M. L.; Langer, J.; Procházka, M.; Tran, V.; Schlücker, S. Towards Reliable and Quantitative Surface-Enhanced Raman Scattering (SERS): From Key Parameters to Good Analytical Practice. *Angew. Chem., Int. Ed.* **2020**, *59*, 5454−5462.

(43) Kopelman, R. Fractal Reaction Kinetics. *Science* **1988**, *241*, 1620−1626.

(44) Yang, G.; Hallinan, D. T. Gold Nanoparticle Monolayers from Sequential Interfacial Ligand Exchange and Migration in a Three-Phase System. *Sci. Rep.* **2016**, *6*, No. 35339.

(45) Mueller, N. S.; Vieira, B. G. M.; Schulz, F.; Kusch, P.; Oddone, V.; Barros, E. B.; Lange, H.; Reich, S. Dark Interlayer Plasmons in Colloidal Gold Nanoparticle Bi- and Few-Layers. *ACS Photonics* **2018**, *5*, 3962−3969.

(46) Vieira, B. G. M.; Mueller, N. S.; Barros, E. B.; Reich, S. Plasmonic Properties of Close-Packed Metallic Nanoparticle Mono- and Bilayers. *J. Phys. Chem. C* **2019**, *123*, 17951−17960.

(47) Green, M. A. Self-Consistent Optical Parameters of Intrinsic Silicon at 300K Including Temperature Coefficients. *Sol. Energy Mater. Sol. Cells* **2008**, *92*, 1305−1310.

(48) Muller, P. Glossary of Terms Used in Physical Organic Chemistry (IUPAC Recommendations 1994). *Pure Appl. Chem.* **1994**, *66*, 1077−1184.

(49) Schürmann, R.; Luxford, T. F. M.; Vinklárek, I. S.; Kočišek, J.; Zawadzki, M.; Bald, I. Interaction of 4-Nitrothiophenol with Low Energy Electrons: Implications for Plasmon Mediated Reactions. *J. Chem. Phys.* **2020**, *153*, No. 104303.

(50) Bald, I.; Langer, J.; Tegeder, P.; Ingólfsson, O. From Isolated Molecules Through Clusters and Condensates to the Building Blocks of Life. *Int. J. Mass Spectrom.* **2008**, *277*, 4−25.

(51) Schürmann, R.; Tanzer, K.; Dąbkowska, I.; Denifl, S.; Bald, I. Stability of the Parent Anion of the Potential Radiosensitizer 8-Bromoadenine Formed by Low-Energy (<3 eV) Electron Attachment. *J. Phys. Chem. B* **2017**, *121*, 5730−5734.

(52) Sala, L.; Sedmidubská, B.; Vinklárek, I. S.; Fárník, M.; Schürmann, R.; Bald, I.; Med, J.; Slavíček, P.; Kočišek, J. Electron Attachment to Microhydrated 4-Nitro- and 4-Bromo-Thiophenol. *Phys. Chem. Chem. Phys.* **2021**, *23*, 18173−18181.

(53) Szczerbiński, J.; Gyr, L.; Kaeslin, J.; Zenobi, R. Plasmon-Driven Photocatalysis Leads to Products Known from E-beam and X-ray-Induced Surface Chemistry. *Nano Lett.* **2018**, *18*, 6740−6749.

(54) Jiang, P.; Dong, Y.; Yang, L.; Zhao, Y.; Xie, W. Hot Electron-Induced Carbon−Halogen Bond Cleavage Monitored by in Situ Surface-Enhanced Raman Spectroscopy. *J. Phys. Chem. C* **2019**, *123*, 16741−16746.

(55) Szafranski, C. A.; Tanner, W.; Laibinis, P. E.; Garrell, R. L. Surface-Enhanced Raman Spectroscopy of Halogenated Aromatic Thiols on Gold Electrodes. *Langmuir* **1998**, *14*, 3580−3589.

(56) Emmons, E. D.; Guicheteau, J. A.; Fountain, A. W.; Tripathi, A. Effect of Substituents on Surface Equilibria of Thiophenols and Isoquinolines on Gold Substrates Studied Using Surface-Enhanced Raman Spectroscopy. *Phys. Chem. Chem. Phys.* **2020**, *22*, 15953−15965.

(57) Biggs, K. B.; Camden, J. P.; Anker, J. N.; van Duyne, R. P. Surface-Enhanced Raman Spectroscopy of Benzenethiol Adsorbed from the Gas Phase onto Silver Film over Nanosphere Surfaces: Determination of the Sticking Probability and Detection Limit Time. *J. Phys. Chem. A* **2009**, *113*, 4581−4586.

(58) Huh, H.; Trinh, H. D.; Lee, D.; Yoon, S. How Does a Plasmon-Induced Hot Charge Carrier Break a C-C Bond? *ACS Appl. Mater. Interfaces* **2019**, *11*, 24715−24724.

(59) Zhang, X.; Mainka, M.; Paneff, F.; Hachmeister, H.; Beyer, A.; Gölzhäuser, A.; Huser, T. Surface-Enhanced Raman Spectroscopy of Carbon Nanomembranes from Aromatic Self-Assembled Monolayers. *Langmuir* **2018**, *34*, 2692−2698.

(60) Adams, D. M.; Brus, L.; Chidsey, C. E. D.; Creager, S.; Creutz, C.; Kagan, C. R.; Kamat, P. V.; Lieberman, M.; Lindsay, S.; Marcus, R. A.; et al. Charge Transfer on the Nanoscale: Current Status. *J. Phys. Chem. B* **2003**, *107*, 6668−6697.

(61) Baffou, G.; Quidant, R.; de Abajo, F. J. G. Nanoscale Control of Optical Heating in Complex Plasmonic Systems. *ACS Nano* **2010**, *4*, 709−716.

(62) Dongare, P. D.; Zhao, Y.; Renard, D.; Yang, J.; Neumann, O.; Metz, J.; Yuan, L.; Alabastri, A.; Nordlander, P.; Halas, N. J. A 3D Plasmonic Antenna-Reactor for Nanoscale Thermal Hotspots and Gradients. *ACS Nano* **2021**, *15*, 8761−8769.

(63) Koopman, W.; Sarhan, R. M.; Stete, F.; Schmitt, C. N. Z.; Bargheer, M. Decoding the Kinetic Limitations of Plasmon Catalysis: The Case of 4-Nitrothiophenol Dimerization. *Nanoscale* **2020**, *12*, 24411−24418.